Cancer Biol Med 2026. doi: 10.20892/j.issn.2095-3941.2025.0691

ORIGINAL ARTICLE

Integrative multi-omic analysis identified *ERBB2* mutations and senescence-driven immune suppression as dual therapeutic targets in LAR triple-negative breast cancer

Yaxin Zhao[1,2], Han Wang[1], Ying Wang[1], Yizhou Jiang[1,2], Xin Hu[1,3]*, Zhiming Shao[1,2]*

[1]Key Laboratory of Breast Cancer in Shanghai, Department of Breast Surgery, Fudan University Shanghai Cancer Center, Shanghai 200032, China; [2]Department of Oncology, Shanghai Medical College, Fudan University, Shanghai 200032, China; [3]Precision Cancer Medical Center Affiliated to Fudan University Shanghai Cancer Center, Shanghai 201315, China

ABSTRACT

Objective: The luminal androgen receptor (LAR) subtype of triple-negative breast cancer (TNBC) differentiation displays low proliferation yet strong metastatic potential and a poor chemotherapy response. This study aimed to define the molecular basis of the LAR subtype and identify actionable therapeutic targets.

Methods: Comprehensive multi-omic analyses were performed on the FUSCC-TNBC cohort, integrating whole-exome sequencing, RNA sequencing, and functional validation *in vitro* and *in vivo*. Somatic mutation profiling, gene set enrichment analysis (GSEA), and weighted gene co-expression network analysis (WGCNA) were used to define genomic and transcriptomic signatures. A machine learning model using the Mime1 package was applied to derive a senescence-associated prognostic signature (LAR-S) and validation in external cohorts. Immune deconvolution was performed to decipher the tumor microenvironment. Functional assays, patient-derived organoids (PDOs), and TS/V mouse models were used to evaluate therapeutic responses to senescence-modulating agent and immunotherapy combinations.

Results: The LAR subtype was enriched for *PIK3CA*, *PTEN*, and *ERBB2* kinase domain mutations. Functional studies confirmed *ERBB2* variants (e.g., V777L and E698_P699delinsA) as oncogenic drivers conferring sensitivity to neratinib. Transcriptomic analyses revealed a dominant cellular senescence program associated with immune suppression. The LAR-S signature stratified survival across cohorts and predicted immunotherapy resistance. Targeting cellular senescence inhibited LAR subtype organoid growth and when combined with anti-PD-1 therapy synergistically suppressed tumor growth *in vivo*.

Conclusions: The LAR subtype harbors two therapeutic vulnerabilities: *ERBB2* mutation-driven kinase activation; and senescence-mediated immune evasion. The LAR-S signature enables precise patient stratification and supports senescence-targeted and immunotherapy combination strategies as promising approaches for this refractory TNBC subtype.

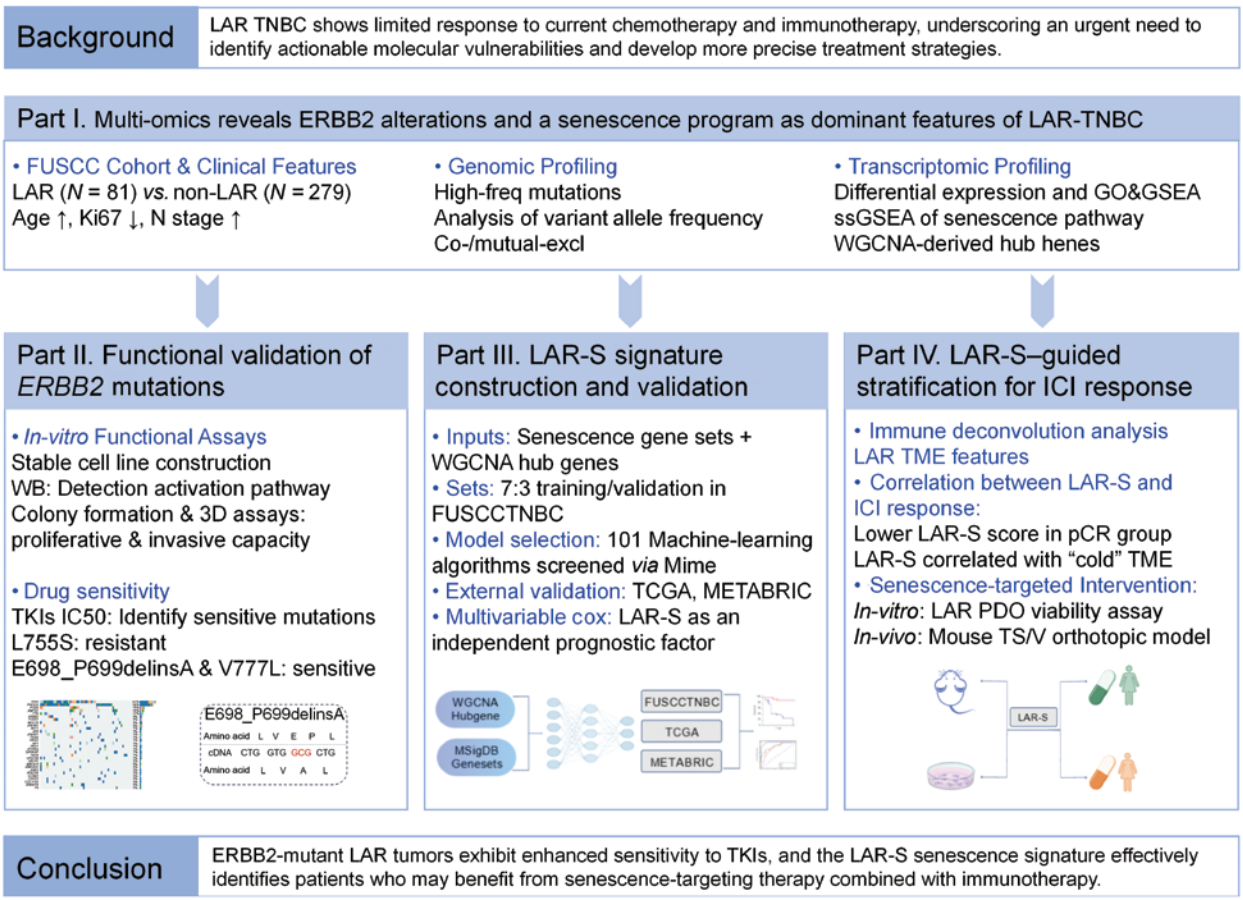
KEYWORDS Triple-negative breast cancer; luminal androgen receptor subtype; *ERBB2* mutation; cellular senescence; immunotherapy resistance

Introduction

Triple-negative breast cancer (TNBC) is an aggressive and highly heterogeneous malignancy that is characterized by the absence of estrogen receptor (ER) and progesterone receptor (PR) expression, and the lack of HER2 overexpression and *ERBB2* amplification[1]. Systemic chemotherapy remains the therapeutic backbone for most patients despite recent advances with immune checkpoint inhibitors (ICIs) and antibody-drug conjugates[2]. However, the efficacy of these treatments is limited, underscoring the urgent need for novel therapeutic strategies rooted in a deeper biological understanding of the disease.

Transcriptomic profiling has been instrumental in dissecting the heterogeneity of TNBC, leading to the identification of distinct molecular subtypes, including the luminal androgen receptor (LAR) subtype[3,4]. The LAR subtype accounts for 10%–20% of all TNBC cases and is characterized by androgen receptor (AR) expression and a luminal gene signature. Clinically, LAR tumors predominantly affect older patients, display a lower Ki-67 proliferation index, and are relatively resistant to conventional neoadjuvant chemotherapy[4-6].

*These authors contributed equally to this work as corresponding authors.
Correspondence to: Xin Hu and Zhiming Shao
E-mail: xinhu@fudan.edu.cn and zhiming_shao@fudan.edu.cn
ORCID ID: https://orcid.org/0000-0002-8160-8362 and https://orcid.org/0000-0002-4503-148X
Received November 11, 2025; accepted February 23, 2026.
Available at www.cancerbiomed.org
©2026 The Authors. Creative Commons Attribution-NonCommercial 4.0 International License (CC BY-NC 4.0)



Study Flowchart Schematic overview of the study design, including cohort selection, multi-omic analyses, functional experiments, signature construction, and therapeutic validation in LAR triple-negative breast cancer.

Consequently, targeting the AR directly has been considered the most logical therapeutic strategy. However, clinical trials with AR antagonists, such as enzalutamide and bicalutamide, have yielded only modest response rates, suggesting that AR signaling is not the sole oncogenic driver in these tumors and that alternative targets are needed[7,8].

Multi-omic analyses of large patient cohorts have begun to uncover these alternative drivers. Notably, a comprehensive genomic and transcriptomic analysis of the Fudan University Shanghai Cancer Center TNBC cohort (FUSCC-TNBC) revealed that somatic mutations in *ERBB2* are significantly and almost exclusively enriched within the LAR subtype[4]. These non-amplified *ERBB2* kinase domain mutations (e.g., L755S and V777L) are known oncogenic drivers that confer sensitivity to HER2-targeted tyrosine kinase inhibitors (TKIs), such as neratinib and pyrotinib[9,10]. This finding highlights a critical, high-priority therapeutic vulnerability in a distinct subset of LAR patients.

In addition to specific genomic alterations, the unique clinical presentation of the LAR subtype is characterized by a low proliferative index yet the high metastatic potential suggests that other biological factors may be involved[3,4]. This paradox aligns with the phenotype of cellular senescence (an irreversible cell cycle arrest that explains the low Ki-67 index) coupled with the acquisition of a potent, pro-inflammatory secretome known as the senescence-associated secretory phenotype (SASP)[11,12]. The SASP is a complex mixture of cytokines, chemokines, and proteases that can profoundly remodel the tumor microenvironment (TME). By recruiting immunosuppressive cells, such as myeloid-derived suppressor cells (MDSCs) and M2-like macrophages, the SASP is a powerful mechanism underlying immune evasion and has been directly linked to therapeutic resistance and metastatic progression[13,14].

Herein we sought to define and target the unique molecular vulnerabilities of the LAR subtype. Enrichment of actionable *ERBB2* mutations was validated based on a comprehensive multi-omic analysis and functional *in vitro* evidence that these mutations confer sensitivity to next-generation TKIs is provided. Furthermore, the LAR transcriptome was shown to be significantly enriched for features of cellular senescence. Building on this finding, a robust, machine learning-derived

senescence-associated prognostic signature that effectively risk-stratifies patients was developed and validated. We hypothesized that this senescent phenotype creates a targetable dependency. Finally, preclinical *in vitro* and *in vivo* evidence is provided supporting dramatic inhibition of tumor growth by combining a senescence inhibitor and anti-PD-1 immunotherapy. The current study deciphers the complex biology of the LAR subtype of TNBC, identifying both *ERBB2* mutations and cellular senescence as cooperative, actionable therapeutic axes for this refractory disease.

Materials and methods

Ethics approval and patient cohorts

The current study included a multi-omics cohort of patients with TNBC from the FUSCC. The FUSCC-TNBC cohort was comprised of 465 patients, of whom 360 had RNA-seq data available, 401 had copy-number alteration (CNA) data available, and 279 had whole-exome sequencing (WES) data available. The cohort and biospecimen collection have been described previously. All tissue samples were obtained after approval by the FUSCC Ethics Committee and each patient provided written informed consent for data and tissue use. At the time of diagnosis, all tumors were reviewed by experienced breast pathologists at FUSCC. TNBC was strictly defined as unilateral invasive ductal carcinoma with an ER-, PR-, and HER2-negative phenotype. ER and PR negativity were defined as <1% positively stained tumor nuclei by immunohistochemistry (IHC), in accordance with the 2010 ASCO/CAP guidelines[15]. HER2 negativity was defined as an IHC score of 0 or 1+, or 2+ without *ERBB2* gene amplification by *in situ* hybridization, according to the same guidelines. Further details about this cohort have been described in our previous study[4]. The Cancer Genome Atlas (TCGA)[16], Molecular Taxonomy of Breast Cancer International Consortium (METABRIC)[17], and I-SPY2[18] cohorts were included for external validation and the data were acquired from cBioportal[19] and the GEO database (GSE194040).

Genomic and transcriptomic data analysis

Somatic mutation data from the FUSCC-TNBC cohort were analyzed using the R package, maftools. Oncoplots were generated to visualize the mutation landscape. The frequencies of high-prevalence mutations were compared between LAR and non-LAR subtypes using Fisher's exact test. Variant allele frequency (VAF) distributions were plotted and somatic interaction analysis (co-occurrence and mutual exclusion) was performed using Fisher's exact test. The gene level of the copy-number variations (CNVs) was obtained by GISTIC2.0. CNV frequencies were compared between LAR and non-LAR tumors using a two-tailed Fisher's exact test to identify LAR-specific CNVs.

Transcriptomic data analysis

Differential gene expression analysis between LAR and non-LAR subtypes was performed using the R package, limma or DESeq2. Gene Ontology (GO)[20] and Kyoto Encyclopedia of Genes and Genomes (KEGG)[21] pathway enrichment analyses on differentially expressed genes (DEGs) were performed using the clusterProfiler[22] package. Gene set enrichment analysis (GSEA) was performed using pre-ranked gene lists against the MSigDB[23] gene set collections. Single-sample GSEA (ssGSEA) was performed using the GSVA R package to calculate enrichment scores for specific pathways for each sample. Weighted gene co-expression network analysis (WGCNA) was performed on the LAR subtype transcriptome using the WGCNA R package to identify modules of co-expressed genes. CIBERSORT and Immuno-Oncology Biological Research (IOBR)[24] were used to investigate the features of the TME.

Human and mouse cell lines

Human breast cancer cell lines (MDA-MB-453 and MCF-10A) were obtained from the American Type Culture Collection [ATCC] (Manassas, VA, USA) and the Guohong Hu laboratory (Shanghai Institute of Nutrition and Health, University of Chinese Academy of Sciences, Shanghai, China), respectively. The TS/A mouse TNBC cell line was obtained from the Yibin Kang laboratory (Princeton University, Princeton, NJ, USA). All cell lines were classified as the TNBC LAR subtype, as previously described[25]. Cell viability, mycoplasma contamination, and short tandem repeat analysis were monitored to identify cell lines. MDA-MB-453 and TS/A cells were maintained in high-glucose DMEM (#L110; Basal Media, Shanghai, China) supplemented with 10% FBS (Gibco, Grand Island, NY, USA) and 1% penicillin-streptomycin (Basal Media, Shanghai, China). MCF-10A cells were maintained in DMEM/F-12 (Gibco, Grand Island, NY, USA) supplemented with 5% horse serum (Gibco, Grand Island, NY, USA), 20 ng/mL EGF (PeproTech, Rocky Hill, NJ, USA), 0.5 μg/mL hydrocortisone (Sigma-Aldrich, St. Louis, MO, USA), 100 ng/mL cholera toxin (Sigma-Aldrich, St. Louis, MO, USA), and 10 μg/mL insulin (Basal Media, Shanghai China) at 37°C in a 5% CO_2 incubator.

Colony formation assays

MDA-MB-453 cells were seeded in a 6-well plate (2×10^3 cells/well) and incubated for 2 weeks. Cells were stained with 0.1% crystal violet (Solarbio, Beijing, China) and washed with phosphate-buffered saline. Colonies containing >50 cells were counted.

In vitro cell viability assays

Cells were plated at optimal seeding densities in 96-well plates and allowed to adhere overnight to perform cell viability assays. The optimal seeding densities were established based on each cell line reaching 75%–80% confluence at the end of the assay. The day after the cells reached confluence, the growth medium was removed and 100 μL of fresh medium containing various inhibitors at corresponding concentrations was added to each well. After 72 h, cell viability was assessed using Cell Counting Kit-8 (#40203ES92; Yeasen). The absorbance was measured at 450 nm (A450).

Three-dimensional (3D) culture and drug testing

3D cultures were established using growth facto-reduced Matrigel (Corning, Bedford, MA, USA). MCF-10A cells were resuspended at 2–5 × 10^4 cells/mL in ice-cold Matrigel and seeded at 2,000–4,000 cells/dome. Cells were seeded on a solidified Matrigel layer and overlaid with 2% Matrigel in assay medium for Matrigel-on-top assays. Cultures were allowed to establish for 3–4 days, then treated with lapatinib, neratinib, afatinib, or pyrotinib (0.5–2 μM; DMSO ≤0.1%) and refreshed every 48–72 h. Phase-contrast images were acquired on days 7–10 using an inverted microscope (CKX53, Olympus, Tokyo, Japan) under identical exposure conditions. Viability was measured using CellTiter-Glo (G9628; Promega, Madison, WI, USA) according to the manufacturer's instructions.

Transplantation models

Female BALB/c and nude BALB/c mice (5–6 weeks old) were obtained from Shanghai Jihui Laboratory Animal Care (Shanghai, China). To establish allograft models, 5 × 10^5 TS/A mouse breast cancer cell lines were injected into the mammary fat pad region of each BALB/c mouse. Mice were housed in a specific pathogen-free facility with individually ventilated cages under 12-h light/dark cycles at an ambient temperature of 20–22°C and humidity of 60 ± 10%. The mice were provided with a standard rodent diet (1010013; Jiangsu Xietong Pharmaceutical Bio-engineering, Jiangsu, China) and water *ad libitum*.

Organoid culture

Human breast cancer organoids were stored in a biobank following a previously published protocol[26]. The organoids were resuscitated from the biobank and resuspended in BME type-2 medium (3533-010-02; Trevigen). Then, the suspension was plated in a 300-μL drop within a 12 mm, 0.4 μm inner Transwell chamber (Corning). The drop was solidified by a 30-min incubation at 37°C and 5% CO_2 with 1 mL of breast cancer organoid medium [(Advanced DMEM/F12 supplemented with R-spondin-1, 500 ng/mL; PeproTech, Rocky Hill, NJ, USA), Noggin (100 ng/mL; PeproTech), 5 nM Neuregulin (PeproTech), 5 nM estradiol (Sigma-Aldrich, St. Louis, MO, USA), 1 mM HEPES (Gibco, Grand Island , NY, USA), 1X GlutaMAX (Gibco), 5 mM nicotinamide (Sigma), N-acetylcysteine (1.25 mM; Sigma), 1X B-27 (Gibco), A83-01 (0.5 mM; Tocris), 1X Primocin (InvivoGen), SB-202190 (500 nM; Selleck Chemicals, Houston, TX, USA), 5 mM Y27632 (Selleck), FGF10 (20 ng/mL; PeproTech), FGF7 (5 ng/mL; PeproTech) and EGF (5 ng/mL; PeproTech)].

In vivo mouse studies

All animal experiments were performed in accordance with protocols approved by the Research Ethical Committee of FUSCC (FUSCC-IACUC-S2025-0679). The *in vivo* experimental protocols were reviewed and approved by the Institutional Animal Care and Use Committee. Mice with transplanted tumors were randomly divided into 4 groups: (1) treatment with 0.2% carboxymethyl cellulose and 0.1% Tween 80; (2) treatment with NMN (300 mg/kg, oral gavage daily); (3) treatment with DMSO plus anti-PD-1 antibody (#BE0146, clone RMP1-14, 200 μg; BioXcell), injected intraperitoneally on days 3, 7, 10, and 14; and (4) treatment with NMN plus anti-PD-1 antibody. Tumor size was measured daily. Tumor volume in mm^3 was calculated using the following formula: tumor volume = 0.5 × L × W^2, where L is the longest dimension and W is the perpendicular dimension. Tumor weights among the four treatment groups (control, anti-PD-1, NMN, and combination) were compared using one-way ANOVA followed by Tukey's *post hoc* multiple-comparison test. Data are presented as the mean ± SEM.

Machine learning signature development

Senescence-related genes derived from the LAR-specific WGCNA modules were used as the initial feature pool for prognostic modeling. Prognostic modeling was performed using the Mime R package, which systematically evaluates 101 combinations of 10 established machine learning algorithms, including random survival forest (RSF), LASSO, Ridge, Elastic Net, gradient boosting machine (GBM), SuperPC, CoxBoost, stepwise Cox regression (StepCox), survival support vector machine (survival-SVM), and partial least squares Cox regression (plsRcox)[27]. The FUSCC-TNBC cohort (n = 360) was randomly split into a training set (70%) and an internal validation set (30%). Hyperparameters for each candidate model were tuned by k-fold cross-validation within the training set and Harrell's concordance index (C-index) was used to quantify predictive performance. The

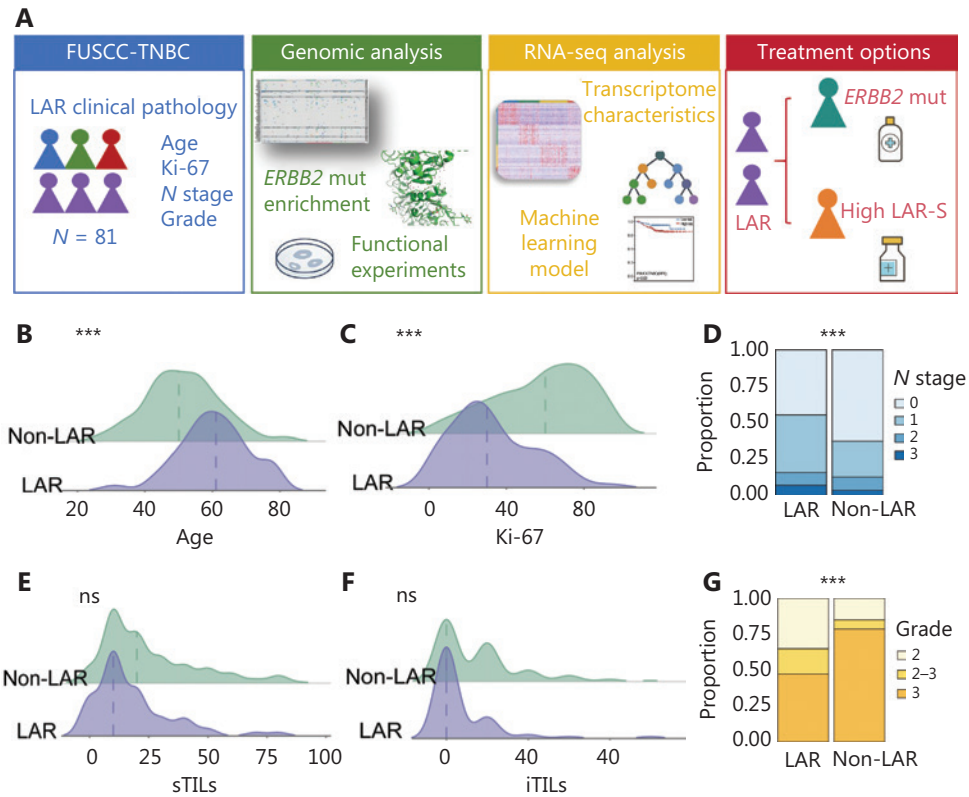


Figure 1 Clinicopathologic characteristics and study workflow for TNBC LAR and non-LAR subtypes. (A) Schematic diagram of the overall study design and analytical workflow. (B, C) Distribution of clinicopathologic variables between LAR and non-LAR subtypes, presented as ridge plots. (B) Patient age at the time of diagnosis, (C) Ki-67 proliferation index. (D) Bar plot demonstrates comparison of lymph node status (*N* stage) between LAR and non-LAR subtypes. (E, F) Distribution of clinicopathologic variables between LAR and non-LAR subtypes, presented as ridge plots of (E) sTILs and (F) iTILs. (G) Bar plot demonstrates comparison of histologic grade (Grade) between LAR and non-LAR subtypes. iTILs, intratumoral tumor-infiltrating lymphocytes; sTILs, stromal tumor-infiltrating lymphocytes. Continuous variables were compared using the Wilcoxon rank-sum test, and categorical variables were compared using the χ^2 or Fisher's exact test, as appropriate. Significance levels are denoted as follows: ns, not significant; *P < 0.05; **P < 0.01; ***P < 0.001; ****P < 0.0001.

algorithmic combination with the highest cross-validated C-index in the training set was selected as the final LAR-S model and subsequently evaluated in the held-out FUSCCT-NBC validation set and in two external TNBC cohorts (TCGA-BRCA and METABRIC) as independent test sets. The final model was used to compute a LAR-S risk score for every patient in each cohort and patients were dichotomized into high- and low-risk groups according to the cohort-specific median LAR-S score.

Quantification and statistical analysis

The normality of continuous variables was assessed using the Shapiro–Wilk test. Differences between two groups were analyzed using the unpaired Student's *t*-test for approximately normally distributed data. The Wilcoxon rank-sum (Mann–Whitney *U*) test was applied for non-normally distributed data. One- or two-way ANOVA followed by Tukey's *post hoc* test was used for comparisons involving more than two groups in *in vitro* drug-sensitivity assays. All cell-based *in vitro* experiments were independently repeated at least three times in triplicate and data are presented as the mean ± SEM unless otherwise indicated in the figure legends. Two-sided P values < 0.05 were considered statistically significant and detailed P values and sample sizes are reported in the main and supplementary figure legends. P values were adjusted for multiple testing using the Benjamini-Hochberg method to control the false discovery rate (FDR) for high-throughput omics data analyses, including differential gene expression, pathway enrichment analysis, and genome-wide mutation frequency comparisons. A significance threshold of adjusted P < 0.05 (or q-value < 0.25 for GSEA, as per standard recommendations) was applied. Raw P values derived from Fisher's exact test or the Wilcoxon rank-sum test are reported for

comparisons of baseline clinical characteristics. All figures were created by R software (http://www.R-project.org, version 3.5.2), Sangerbox Tools[28], and BioGDP[29]. All statistical analyses were performed with R software or GraphPad Prism software (version 9.0).

Result

Clinical and pathologic characteristics of TNBC patients with LAR and non-LAR subtypes

The study design and analytical workflow are summarized in **Figure 1A**. We first analyzed and compared the clinicopathologic characteristics between patients with LAR and non-LAR subtypes. Significant differences were demonstrated between the two groups with respect to age at the time of diagnosis, menopausal status, histologic grade, Ki-67 proliferation index, and lymph node status.

Patients with the LAR subtype were generally older with 51.85% diagnosed at >60 years of age compared to 19.71% in the non-LAR subtype ($P < 0.001$; **Table S1**). Consequently, most LAR cases occurred in postmenopausal women, whereas pre- and post-menopausal cases were nearly equal among non-LAR patients (80.25% *vs.* 56.99%; $P < 0.001$). Analysis of the Ki-67 proliferation index showed that LAR tumors exhibited a significantly lower proliferative activity than non-LAR tumors. Among LAR patients, 17.28% had a Ki-67 index <14% compared to 5.02% in non-LAR cases ($P < 0.001$). Despite this lower proliferative index, no significant difference was detected in tumor size between the two groups (35.80% *vs.* 36.56%; $P = 1$). Greater than one-half of the LAR tumors had lymph node metastasis (54.32%), whereas only 35.48% of non-LAR cases exhibited nodal involvement ($P < 0.001$). These findings collectively suggested that the LAR subtype is associated with older age, postmenopausal status, better differentiation, lower proliferative activity, and a higher likelihood of lymph node metastasis compared to the non-LAR subtype, while showing no significant differences in stromal tumor-infiltrating lymphocytes (sTILs) and intratumoral tumor-infiltrating lymphocytes (iTILs). Although TNBCs are generally characterized by poor differentiation, there was a significant difference in histologic grade distribution between the two subtypes (**Figure 1B – 1G**). In the LAR group, 32.10% of tumors were grade ≤2 compared to only 13.62% in the non-LAR group ($P < 0.001$), indicating that LAR tumors are more likely to be well-differentiated. In LAR patients with WES data, *ERBB2*-mutant tumors alone exhibited a non-significant trend toward occurrence in older, post-menopausal women compared to *ERBB2* wild-type cases with no clear differences in tumor size, Ki-67, grade or nodal status, which likely reflected the limited number of mutant cases (**Table S2**).

Genomic landscape of the TNBC LAR subtype and comparison with the non-LAR subtype

The somatic mutation landscapes of 56 LAR tumors were characterized and compared to 188 non-LAR tumors to delineate the genomic drivers of the LAR subtype (**Figures 2A and S1A**). The overall landscape of the LAR subtype was dominated by high-frequency mutations in *TP53* (61%), *PIK3CA* (50%), *PTEN* (18%), *KMT2C* (16%), and *TTN* (12%). Next, a comparative analysis of mutation frequencies between the two subtypes was performed (**Figure 2B**). This analysis revealed a striking enrichment of oncogenic mutations within the LAR cohort. Most notably, activating mutations in *PIK3CA* were significantly more prevalent in the LAR subtype than in the non-LAR subtype (50% *vs.* 9%; $P < 0.001$). Furthermore, somatic mutations in *ERBB2*, a clinically actionable target, were identified in 9% of LAR cases but were completely absent from the non-LAR group ($P < 0.001$; **Table S3**) and additional *ERBB2* mutations from TCGA selected for functional validation based on their in-frame structural alterations. Conversely, *TP53* mutations, while common in both subtypes, were significantly less frequent in LAR tumors compared to non-LAR tumors (61% *vs.* 79%; $P = 0.008$).

Despite these differences in specific driver genes, the overall tumor mutation burden (TMB) was not significantly different between the two subtypes with a median TMB of 0.84 mutations/Mb in the LAR group and 1.18 mutations/Mb in the non-LAR group (**Figure S1B and S1C**). Analysis of the VAF demonstrated that key driver mutations, including *TP53*, *PIK3CA*, and *ERBB2*, exhibited a median VAF between 0.2 and 0.5, suggesting that these are clonal events, in contrast to the broader VAF distribution in the non-LAR subtype (**Figures 2C and S1D**). Somatic interaction analysis within the LAR cohort revealed patterns of co-mutation and mutual exclusivity (**Figures 2D and S1E**). A significant co-occurrence was noted between mutations in *ATR* and *TTN* ($P < 0.01$), two critical components of the DNA damage response and PI3K signaling pathways, respectively.

The genomic and transcriptomic status of key genes within the PI3K-AKT-mTOR signaling pathway were investigated given the profound enrichment of *PIK3CA* mutations. CNV analysis revealed that the LAR subtype exhibited a significantly lower frequency of copy number loss and deletion in *PIK3R1* compared to the non-LAR group. In addition, the LAR subtype displayed a higher frequency of *PDPK1* and *AKT1* gains and amplifications (**Figure 2E**). mRNA expression analysis confirmed activation of this pathway at the transcriptomic level, which was consistent with the genomic data (**Figure 2F**). *PIK3R1*, *PDPK1*, *AKT1*, *TSC2*, and *MTOR* expression was, on average, significantly higher in the LAR subtype than the non-LAR subtype ($P < 0.001$ for all), supporting the hypothesis that dysregulation of the PI3K-AKT pathway is a hallmark characteristic of the TNBC LAR subtype.

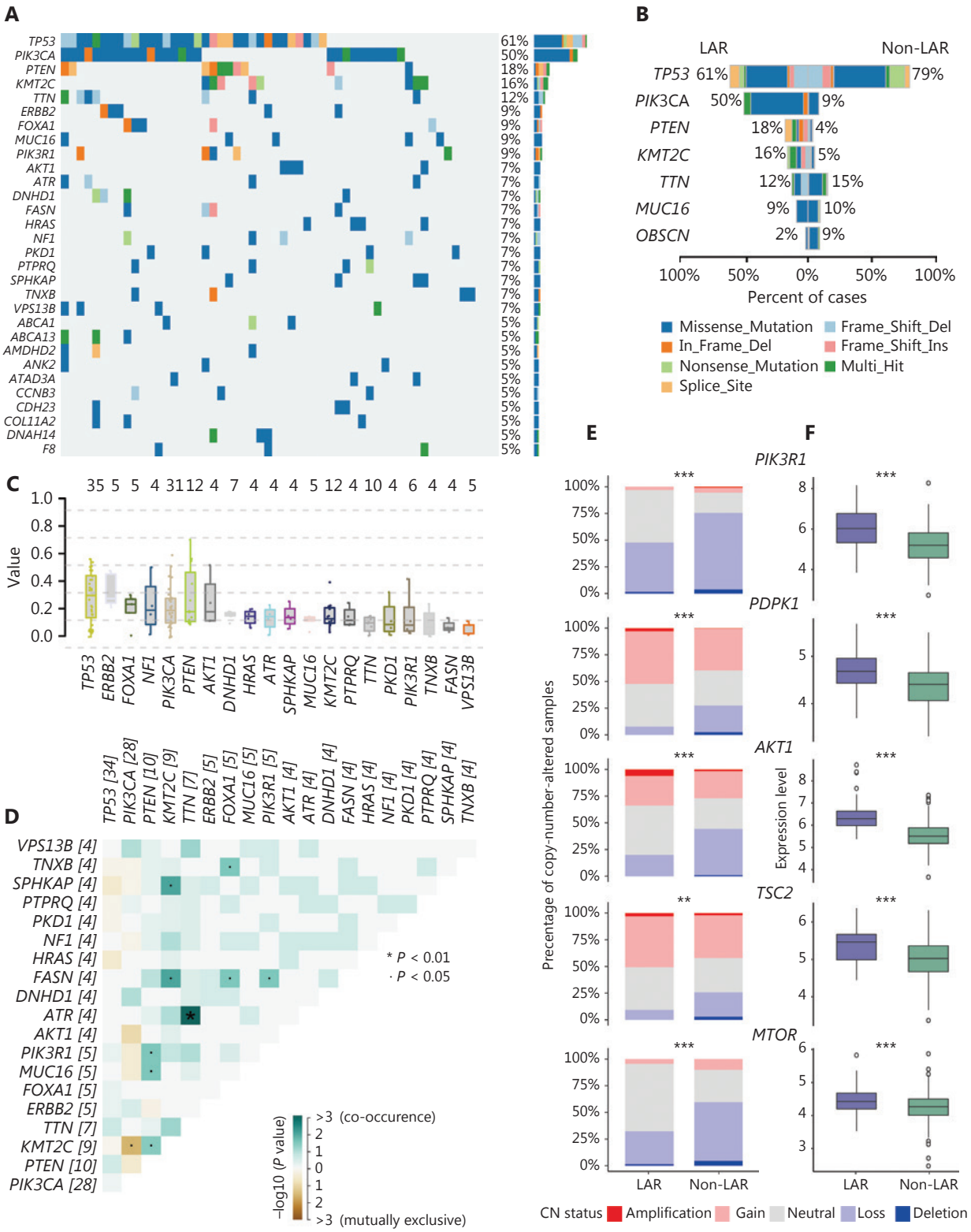


Figure 2 Genomic landscape of the LAR subtype of TNBC and multi-omic analysis of the PI3K-AKT pathway. (A) Oncoplot visualizing the somatic mutation landscape of the LAR subtype. (B) Bar plot comparing the high-frequency mutations between the LAR and non-LAR subtypes. (C) VAFs for key driver mutations identified in the LAR subtype. (D) Correlation heatmap illustrating patterns of co-occurrence and

mutual exclusivity among frequently mutated genes in the LAR subtype. (E) Proportional stacked bar plot comparing the distribution of CNV status (amplification, gain, neutral, loss, and deletion) for key PI3K-AKT pathway genes (*PIK3R1*, *PDPK1*, *AKT1*, *KMT2C*, and *MTOR*) between LAR and non-LAR subtypes. (F) Boxplots comparing the corresponding mRNA expression of the PI3K-AKT pathway genes from the LAR and non-LAR subtypes. CNV, copy number variation; VAFs, variant allele frequencies. Significance of mutation frequency differences was determined by Fisher's exact test with *P* values adjusted using the Benjamini-Hochberg method to control the FDR. Significance levels are denoted as follows: ns, not significant; *$P < 0.05$; **$P < 0.01$; ***$P < 0.001$; ****$P < 0.0001$.

Functional validation of ERBB2 mutations in LAR models identifies differential pathway activation and TKI response

Based on the finding that *ERBB2* somatic mutations are significantly enriched in the LAR subtype, we next sought to functionally characterize these specific mutations. Stable *ERBB2*-mutant lines were generated in the LAR cell context (MDA-MB-453) and in MCF-10A to interrogate signaling output, growth phenotypes, and TKI response.

First, we assessed activation of the HER2 signaling pathway *via* western blot. All tested mutations increased HER2-axis phosphorylation to varying degrees (**Figure 3A**). In MDA-MB-453 cells, V777L and L755S enhanced HER2 Tyr1221 and downstream AKT Ser473 phosphorylation with minimal effect on HER2 Tyr1248. D769Y increased both Tyr1221/Tyr1248 and augmented PLCγ Tyr783 and p44/42. MAPK Thr202, E698_P699delinsA, and Y1127_A1129del boosted Tyr1221/Tyr1248 and PLCγ phosphorylation. G660_V665dup preferentially enhanced Tyr1248, PLCγ, and p44/42 MAPK. In MCF-10A cells, V777L, D769Y, and G660_V665dup robustly increased Tyr1221/Tyr1248 and PLCγ. L755S as well as E698_P699delinsA produced moderate increases with downstream AKT activation. These data collectively supported E698_P699delinsA, V777L, and L755S as activating alterations in this setting. An immunofluorescence assay showed that *ERBB2* mutations had no significant effect on the subcellular localization of the HER2 protein (**Figure S1F**).

The oncogenic potential of these mutations was investigated next. E698_P699delinsA, V777L, L755S, and D769Y markedly increased clonogenic growth in MDA-MB-453 cells, whereas G660_V665dup and Y1127_A1129del had a minimal impact (**Figure 3B and 3C**). In 3D spheroid cultures, which better mimic *in vivo* growth conditions, L755S enhanced spheroid formation in MCF-10A cells and E698_P699delinsA induced an irregular, dysmorphic acinar structure consistent with a more aggressive phenotype. V777L/Y1127_A1129del/G660_V665dup produced spheroids comparable to wild-type (**Figure 3D and 3E**).

Finally, the therapeutic potential of four different HER2 TKIs against these activating mutations was assessed. Drug sensitivity assays in MDA-MB-453 cells revealed distinct response profiles. All mutations, except L755S, conferred sensitivity to lapatinib. Conversely, all mutations, except D769Y, showed sensitivity to neratinib, with V777L and Y1127_A1129del the most sensitive. No significant inhibition was observed for afatinib or pyrotinib across any of the mutant cell lines (**Table S4**).

Taken together, these results functionally validated *ERBB2* mutations in the LAR subtype as oncogenic drivers that activate HER2 signaling and promote malignant growth. Indeed, *ERBB2* mutations confer distinct sensitivity and resistance patterns to TKIs, identifying L755S as a potential lapatinib-resistance mutation and highlighting neratinib as a promising agent for other LAR-associated *ERBB2* mutants, including the novel, highly aggressive E698_P699delinsA mutation.

The TNBC LAR subtype is characterized by a senescent phenotype and an immune-suppressed microenvironment

Although actionable *ERBB2* mutations constitute a key vulnerability in a subset of LAR tumors, the relatively low prevalence prompted us to interrogate the broader transcriptomic landscape to identify therapeutic targets with wider applicability.

GSEA was performed on the differential expression between the LAR and non-LAR subtypes, which revealed that in addition to the expected upregulation of the androgen response pathway (NES = 2.39; $P < 0.001$), LAR tumors were significantly enriched for metabolic pathways, including fatty acid metabolism (NES = 2.30; $P < 0.001$) and bile acid metabolism (NES = 1.96; $P < 0.001$; **Figure 4A**). Conversely, pathways related to the cell cycle and MYC targets were significantly downregulated in LAR tumors (**Figure 4B**). GO analysis further confirmed this metabolic reprogramming, showing upregulation of pathways, such as tyrosine metabolism and steroid hormone biosynthesis (**Figure S1G and S1H**).

We hypothesized that these tumors are characterized by a cellular senescence program given that the LAR subtype patients are often older and have a chemoresistant phenotype. We first examined the expression of key genes associated with the SASP. A differential expression heatmap and bubble plot confirmed that multiple canonical SASP genes (e.g., *IL-6*, *IL-8*, *IL-1A*, *MMP3*, and *CSF2*) were upregulated in the LAR subtype relative to the non-LAR subtype (**Figure 4C**). To validate this at the pathway level, ssGSEA was performed using senescence-associated gene sets from MSigDB. This analysis demonstrated that scores for GOBP cellular, WP cell, and

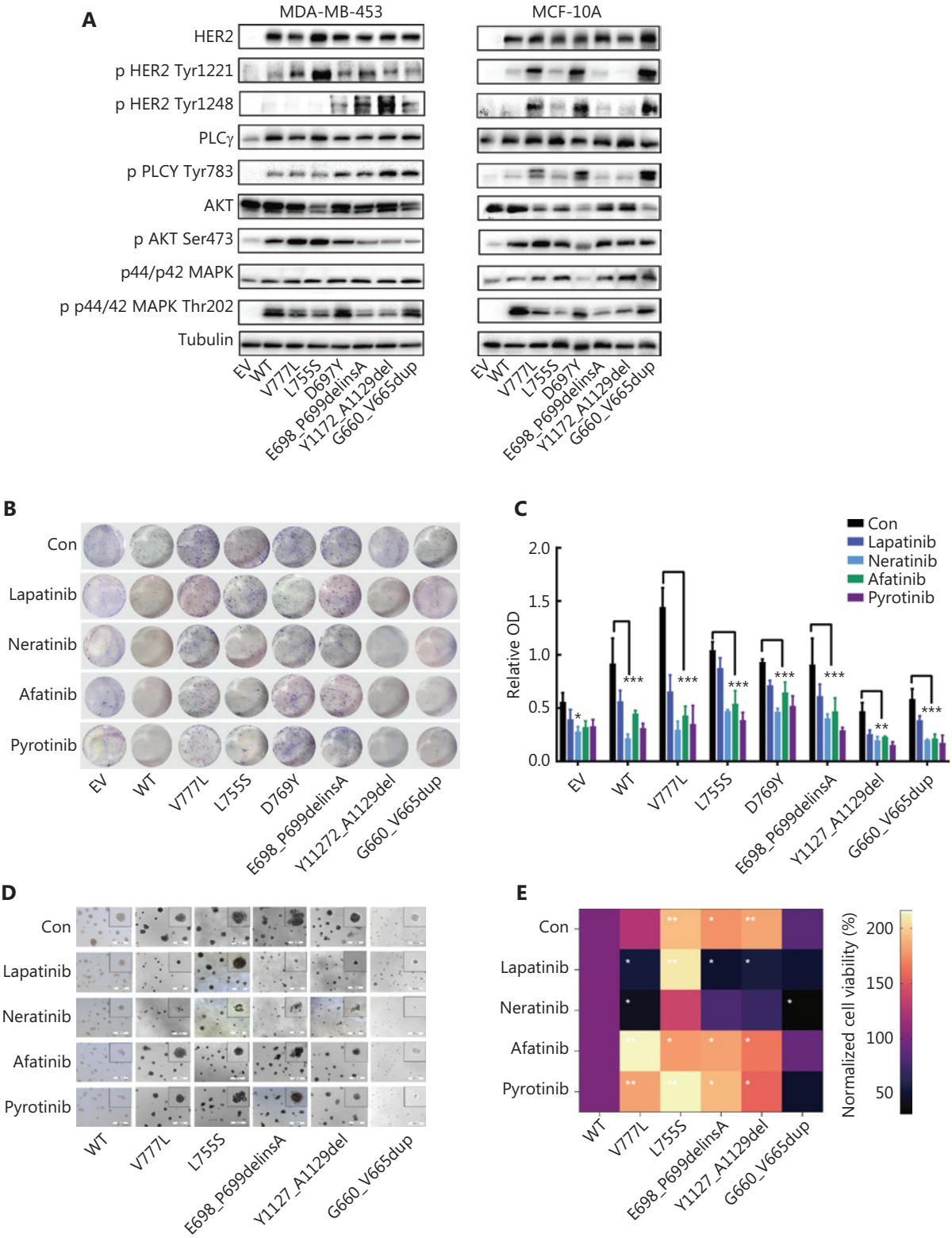


Figure 3 Functional validation and therapeutic targeting of LAR-associated *ERBB2* mutations. (A) Western blot analysis of HER2-PI3K-AKT pathway activation in MDA-MB-453 and MCF-10A cell lines stably expressing empty vector (EV), wild-type (WT) *ERBB2*, or specified *ERBB2* mutations. (B) Representative images of colony formation assays for MDA-MB-453 cells expressing EV, WT *ERBB2*, or *ERBB2* mutations,

assessing oncogenic transformation potential. (C) Bar plot quantifying the colony formation. Data are presented as the mean ± SD from three independent experiments. (D) Representative images of 3D spheroid cultures of MCF-10A cells harboring different *ERBB2* constructs, treated with vehicle (DMSO) or a panel of HER2 TKIs (lapatinib, neratinib, afatinib, and pyrotinib). (E) Heatmap summarizing relative viability under TKI treatment 3D spheroid cultures. EV, empty vector; WT, wild-type; TKIs, tyrosine kinase inhibitors. Data are presented as mean ± SD. Statistical significance was determined using one-way ANOVA followed by Tukey's multiple comparisons test. Significance levels are denoted as follows: ns, not significant; *P < 0.05; **P < 0.01; ***P < 0.001; ****P < 0.0001. Scale bar: 200 μm.

Reactome cellular senescence were significantly elevated in LAR tumors (**Figure 4D–F**). In contrast, pathways indicating negative regulation of senescence were decreased (**Figure 4G**).

To further delineate the intrinsic biology of the LAR subtype and its relation to senescence and prognosis, WGCNA was performed exclusively on LAR tumor transcriptomes. This analysis identified distinct modules of highly co-expressed genes. Module eigengenes (MEs) were correlated with clinical traits and key modules associated with LAR features and relapse-free survival (RFS) were identified (**Figure 4H**). Enrichment-network analysis was then performed on hub genes from these clinically relevant modules. This analysis revealed two biological super clusters. The first cluster was strongly enriched for senescence-associated processes, including DNA-damage checkpoint, cell-cycle arrest, and histone modification/chromatin organization. The second cluster was characterized by profound downregulation of immune pathways. Key processes, including T-cell activation, B cell-mediated immunity, and regulation of type I interferon production, were negatively correlated with the senescent phenotype (**Figure 4I**).

Taken together, these transcriptomic analyses converge on a key finding. Specifically, the LAR subtype is defined by a robust cellular senescence program coupled to a "cold," immunosuppressed TME. This dual phenotype may underlie the characteristic low proliferation, high metastatic potential, and chemoresistance of the TNBC LAR subtype.

Development and validation of a LAR-senescence signature (LAR-S)

Based on the transcriptomic findings that the LAR subtype exhibits a robust cellular senescence program, we sought to develop a prognostic signature derived from these senescence-associated genes from MsigDB (**Table S5**). The FUSCC-TNBC cohort was used as the discovery dataset, randomly partitioning the cohort into a training set (70%) and an internal validation set (30%). An extensive machine-learning pipeline with the Mime package was used to evaluate 101 survival modeling algorithm combinations. The concordance index (C-index) for each model in the training and validation sets is shown in **Figure 5A**. The LASSO + random survival forest (RSF) combination was selected as the optimal model and yielded the LAR-S signature, demonstrating robust predictive performance (C-index = 0.89 in the training set; C-index = 0.68 in the internal validation set). To identify the most critical drivers within this signature, the variable importance (VIMP) derived from the optimal RSF model was analyzed (**Figure 5B**). The analysis revealed that genes, such as *LTC4S*, *PDHA2*, *MYL4*, *ABCG4*, and *RRP8*, were among the top contributors to the predictive accuracy of the model (**Table S6**).

We next validated the prognostic performance of the LAR-S score. Patients in each cohort were stratified into high- and low-risk groups based on the optimal cut-off derived from the FUSCC-TNBC training set. Kaplan–Meier analysis confirmed that low-risk patients had significantly better relapse-free survival (RFS) in the FUSCC-TNBC cohort (P = 0.03, HR = 0.44, 95% CI = 0.21–0.95; **Figure 5C**). The prognostic value of the signature was independently validated in two external cohorts. Low-risk patients showed significantly better overall survival (OS) in the TCGA cohort (P = 0.01, HR = 0.35, 95% CI = 0.15–0.82; **Figure 5D**) and the METABRIC cohort (P = 0.02, HR = 0.67, 95% CI = 0.48–0.94; **Figure 5E**). To further assess whether the LAR-S signature serves as an independent prognostic indicator, multivariate Cox regression analysis was performed incorporating key clinicopathologic factors and molecular subtype (**Figure 5F**). The LAR-S score remained a significant predictor of relapse-free survival (HR = 1.33, 95% CI = 1.02–1.64; P < 0.05), independent of traditional clinical parameters. These findings confirmed that the LAR-S signature captures prognostic information beyond conventional pathologic variables and can serve as a robust, independent biomarker for outcome stratification in TNBC.

Finally, the association between the LAR-S signature and established molecular subtypes was investigated. The high-risk LAR-S group was predominantly composed of LAR tumors in the FUSCC-TNBC cohort (78.5%), whereas the low-risk group was enriched for non-LAR tumors (81.5%; **Figure 5G**). This association was validated in the TCGA cohort, where 71.5% of LAR tumors were high-risk and 76.5% of non-LAR tumors were low risk (**Figure 5H**).

Immune contexture of LAR tumors and clinical implications of the LAR-S signature

The immune landscape of the LAR subtype was investigated given that the LAR-S signature is derived from senescence-associated genes, which are known to modulate the TME. The IOBR package was used to analyze bulk transcriptomic

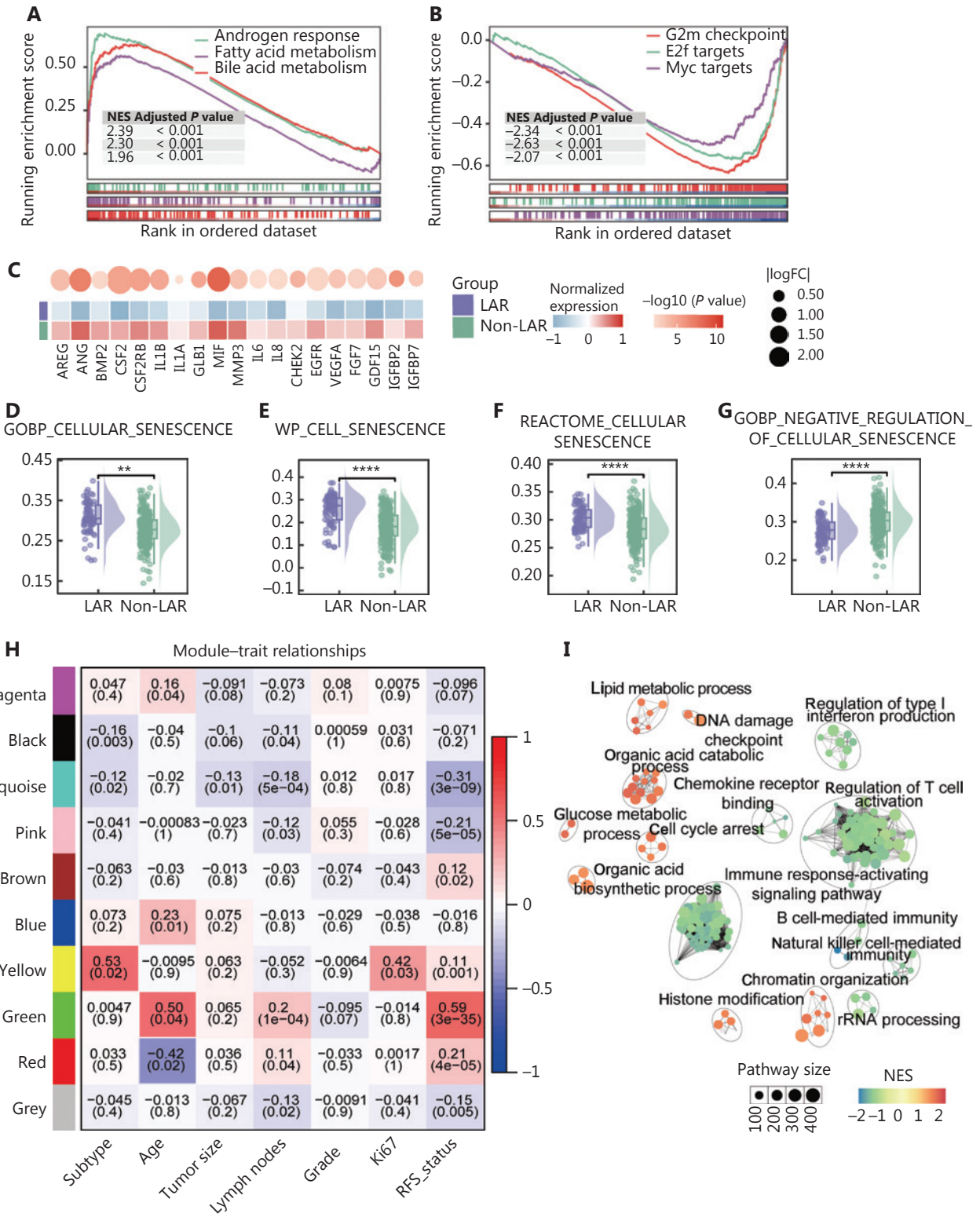


Figure 4 Transcriptomic profiling reveals a distinct cellular senescence signature in the LAR subtype. (A, B) GSEA plots for representative hallmark pathways (A) upregulation and (B) downregulation in the LAR subtype compared to the non-LAR subtype. Significant pathways were identified based on an FDR q-value < 0.25. (C) Expression analysis of SASP genes. Left: Heatmap displaying the normalized expression of SASP

genes across LAR and non-LAR samples. Right: Bubble plot visualizing the log_2FC for each SASP gene. DEGs were defined by a $|log_2FC| > 1$ and an FDR-adjusted $P < 0.05$. (D–G) Boxplots comparing the ssGSEA enrichment scores for senescence-related gene sets: (D) GO BP: cellular senescence; (E) WikiPathways: cell senescence; (F) Reactome: cellular senescence; (G) GO BP: negative regulation of cellular senescence from MSigDB between LAR and non-LAR subtypes. (H) WGCNA performed on the LAR subtype cohort. The heatmap displays the Pearson correlation coefficients and corresponding *P* values for module eigengenes (MEs, rows) against clinicopathological traits (columns). (I) Functional enrichment network of genes within the senescence-associated module. Nodes represent enriched pathways, sized by significance, and edges indicate gene overlap between terms. GSEA, gene set enrichment analysis; SASP, senescence-associated secretory phenotype; ssGSEA, single-sample GSEA; WGCNA, weighted gene co-expression network analysis. Significance levels are denoted as follows: ns, not significant; *$P < 0.05$; **$P < 0.01$; ***$P < 0.001$; ****$P < 0.0001$.

data using multiple deconvolution algorithms (CIBERSORT, EPIC, MCP, and TIMER). This analysis revealed that the LAR subtype generally exhibits an immunosuppressed phenotype that is characterized by significantly lower infiltration of immune-activating cells, such as NK and $CD8^+$ T cells, compared to the non-LAR subtype (**Figure 6A**).

We hypothesized that the LAR-S signature, which is strongly correlated with the LAR subtype (**Figure 5F and 5G**), could serve as a surrogate of this immunosuppressed state and predict response to immunotherapy. Furthermore, we analyzed the publicly available I-SPY2 clinical trial cohort, focusing on TNBC patients who received ICI therapy. We first compared LAR-S scores between patients who achieved a pathologic complete response (pCR) and those who did not (non-pCR). As hypothesized, the non-pCR group exhibited significantly higher LAR-S scores than the pCR group ($P < 0.001$), indicating that a high senescence score is associated with reduced ICIs responsiveness (**Figure 6B**). To probe the biological basis of this reduced responsiveness, we visualized ssGSEA scores for the LAR-S signature and multiple canonical senescence-associated pathways, including SASP, senescence and autophagy in the I-SPY2 cohort. The heatmap demonstrated that non-pCR patients consistently displayed higher enrichment across senescence-related pathways than pCR patients (**Figure 6C**). We then explored the relationship between LAR-S and TME immune pathways specifically within the pCR group. Correlation analysis revealed a negative association between LAR-S and immune-activating pathways (**Figure 6D**). Specifically, higher LAR-S scores correlated with lower T-cell mediated immunity, an IFN-γ response, and STAT1 signaling ($P < 0.05$). These findings reinforce the notion that the senescence signature captures a TME phenotype characterized by profound immunosuppression and attenuated T-cell activation, which helps explain the reduced ICI responsiveness.

Based on the finding that the high-risk LAR phenotype is characterized by both senescence and immunosuppression, we hypothesized that pharmacologic modulation of senescence could resensitize LAR tumors to immunotherapy. First, LAR patient-derived organoids (PDOs) were collected from our center and drug-sensitivity assays were performed. Treatment with a senescence-targeting agent significantly reduced viability and inhibited growth in LAR subtype PDOs, supporting a dependency on the senescent state (**Figure 6E and 6F**). Finally, this finding was translated *in vivo* using a TS/V orthotopic xenograft model. Mice were treated with vehicle control, NMN (an NAD^+ precursor used here as a senescence-modulating agent), anti-PD-1, or the combination of NMN plus anti-PD-1 therapy. While both monotherapies partially delayed progression, the combination produced a markedly greater suppression of tumor growth. The tumor weight in the combination group was significantly lower than the control ($P < 0.0001$), and anti-PD-1 ($P < 0.0001$) and NMN monotherapy groups ($P = 0.0007$) at the endpoint, whereas the difference between anti-PD-1 and NMN alone was not significant ($P = 0.52$), indicating that senescence modulation with NMN can overcome resistance and synergize with anti-PD-1 checkpoint blockade in LAR tumors (**Figure 6G–I**).

Discussion

TNBC presents a significant clinical challenge due to inherent heterogeneity and aggressive nature. The identification of molecular subtypes, including the LAR subtype, has been a critical step towards precision oncology. However, the LAR subtype remains an enigma. Specifically, the LAR subtype is clinically defined by features of lower proliferation (low Ki-67) and older age, yet the LAR subtype exhibits high rates of lymph node metastasis and profound resistance to conventional neoadjuvant chemotherapy[30]. This paradox highlights a clear unmet need for effective, subtype-specific therapeutic strategies.

The most intuitive target in LAR subtype, the AR, has unfortunately been shown limited efficacy in clinical trials. Studies with AR antagonists, like enzalutamide, bicalutamide, and darolutamide, have resulted in only modest response rates [clinical benefit rate (CBR) < 30%], suggesting AR signaling is not the sole oncogenic driver, especially when patients are selected by AR IHC positivity alone[7,8,31]. Other strategies targeting associated pathways, such as CDK4/6 or PI3K inhibitors, are also under active investigation but have not yet become a standard of care, further necessitating the discovery of novel therapeutic vulnerabilities[32-34].

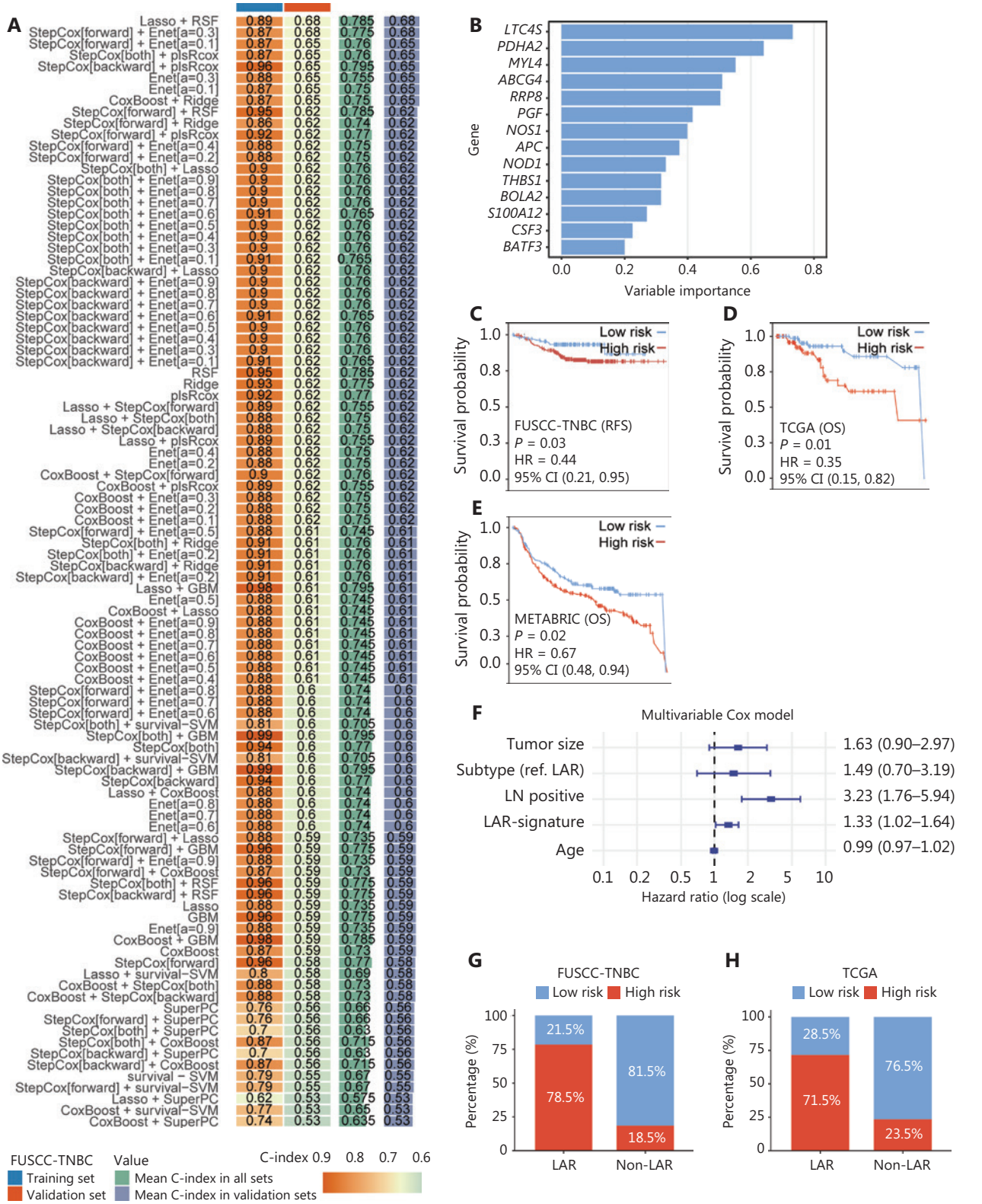


Figure 5 Development and validation of a LAR-senescence signature (LAR-S). (A) Heatmap illustrating the performance of 101 machine learning model combinations, evaluated *via* 10-fold cross-validation in the training cohort to identify the optimal algorithm for signature

construction based on senescence-related genes. (B) Bar plot of the top-ranked genes from the final prognostic model, ranked by VIMP for RFS. (C) Kaplan–Meier analysis of RFS for patients in the FUSCC-TNBC cohort, stratified into high- and low-risk groups by the optimal cut-off of the LAR-S score. (D, E) Kaplan–Meier analysis of OS validating the prognostic power of the LAR-S in the (D) TCGA cohort and (E) METABRIC cohort. (F) Multivariate Cox regression analysis incorporating tumor size, lymph-node status, age, molecular subtype (ref. LAR), and LAR-S signature. (G, H) Proportional stacked bar plot validating the association between LAR-S groups and subtypes in the (G) FUSCC-TNBC and (H) TCGA cohort. OS, overall survival; RFS, relapse-free survival; VIMP, variable importance. Significance levels are denoted as follows: ns, not significant; *P < 0.05; **P < 0.01; ***P < 0.001; ****P < 0.0001.

In this study we performed a comprehensive multi-omic and functional analysis to decipher the unique biology of the TNBC LAR subtype and identified new actionable targets. We uncovered two distinct, therapeutically relevant axes. First, validating and extending the foundational work by Jiang et al.[4], we confirmed that a subset of LAR tumors (9% in our cohort) is uniquely enriched for somatic *ERBB2* mutations (**Figures 2A and S1A**). Importantly, these are non-amplified kinase domain mutations, distinct from the typical HER2+ breast cancer. Our functional analyses demonstrated that these mutations are not passenger events. In fact, these mutations are *bona fide* oncogenic drivers that differentially activate the PI3K-AKT and PLCγ-MAPK pathways. These mutations confer distinct sensitivity profiles to HER2-targeted TKIs (**Figure 3D and 3E**, **Table S4**). For example, we identified L755S as a potential lapatinib-resistance mutation, while confirming V777L and the novel mutation, E698_P699delinsA, as sensitive to neratinib. This finding has immediate translational implications because and suggests that genomic screening for *ERBB2* mutations, a practice not standard in HER2-negative disease, could identify a significant fraction of LAR patients who may benefit from existing TKIs. This finding aligns with the growing recognition of *ERBB2* mutations as actionable targets across various "HER2-low" or "-negative" solid tumors[35,36]. Importantly, the *ERBB2* alterations observed in the FUSCC-TNBC cohort arise in *ERBB2* non-amplified TNBC and are biologically distinct from classical HER2-positive breast cancer driven by *ERBB2* gene amplification and HER2 protein-overexpression. High-level receptor overexpression promotes ligand-independent HER2 dimerization in *ERBB2*-amplified tumors and broad activation of PI3K-AKT and RAS-MAPK signaling, which is optimally targeted by trastuzumab-based antibody regimens. By contrast, the TNBC LAR subtype in the current study harbors somatic kinase-domain *ERBB2* mutations (for example, L755S and V777L) in the context of normal copy number, which is consistent with prior reports of activating HER2 mutations in HER2-negative breast cancer and associated with a distinct pattern of TKI sensitivity. Our functional data therefore support TKI-based precision therapy specifically for the *ERBB2* mutant (*ERBB2* non-amplified TNBC LAR subtype), rather than extrapolation of antibody-based strategies used for *ERBB2*-amplified disease.

While *ERBB2* mutations offer a clear path for a subset of patients, most LAR tumors lack this specific alteration. This prompted us to investigate the broader biological state that defines the LAR subtype. Our transcriptomic analysis provided a compelling answer. The LAR subtype is characterized by a robust cellular senescence program. This finding mechanistically links several subtype-defining clinical features. The enrichment of pathways for cell cycle arrest, DNA damage checkpoint, and lipid metabolism[37] associated with cellular senescence directly explains the low Ki-67 index and inherent resistance to cycle-dependent chemotherapy. Furthermore, upregulation of a potent SASP provides a powerful explanation for the subtype aggressive, metastatic behavior. The SASP is known to remodel the TME by secreting inflammatory cytokines and proteases that promote invasion and angiogenesis[38].

A critical consequence of this senescent phenotype, which we identified through WGCNA, is the establishment of an immune-suppressed or "cold" TME (**Figure 4I**). Our analysis showed that the senescence-associated modules were negatively correlated with T-cell activation, B-cell immunity, and Type I interferon responses. This was further validated by deconvolution analysis, which confirmed that LAR tumors have lower infiltration of activating immune cells, such as M1 macrophages and $CD8^+$ T cells, compared to non-LAR subtypes (**Figure 6A**). This SASP-driven immune exclusion provides a strong biological rationale for the poor response of LAR tumors not only to chemotherapy but also to ICIs.

Based on this central finding, we developed and validated a machine learning-derived LAR-senescence signature (LAR-S). This signature proved to be a robust prognostic tool, successfully stratifying patients into high- and low-risk groups in our FUSCC-TNBC cohort (RFS, $P = 0.03$) and in two independent external cohorts [TCGA (OS; $P = 0.01$) and METABRIC (OS; $P = 0.02$); **Figure 5C–E**]. More importantly than the prognostic value, the LAR-S score functions as a predictive biomarker. Biologically, the top-weighted genes in the LAR-S signature capture the intrinsic features of the senescent, androgen-dependent state. For example, LTC4S and ABCG4 which can shape membrane signaling, inflammatory mediator production and SASP composition. PDHA2 and ABCG4 are implicated in mitochondrial respiration and sterol-transport, respectively. RNA processing and translational control

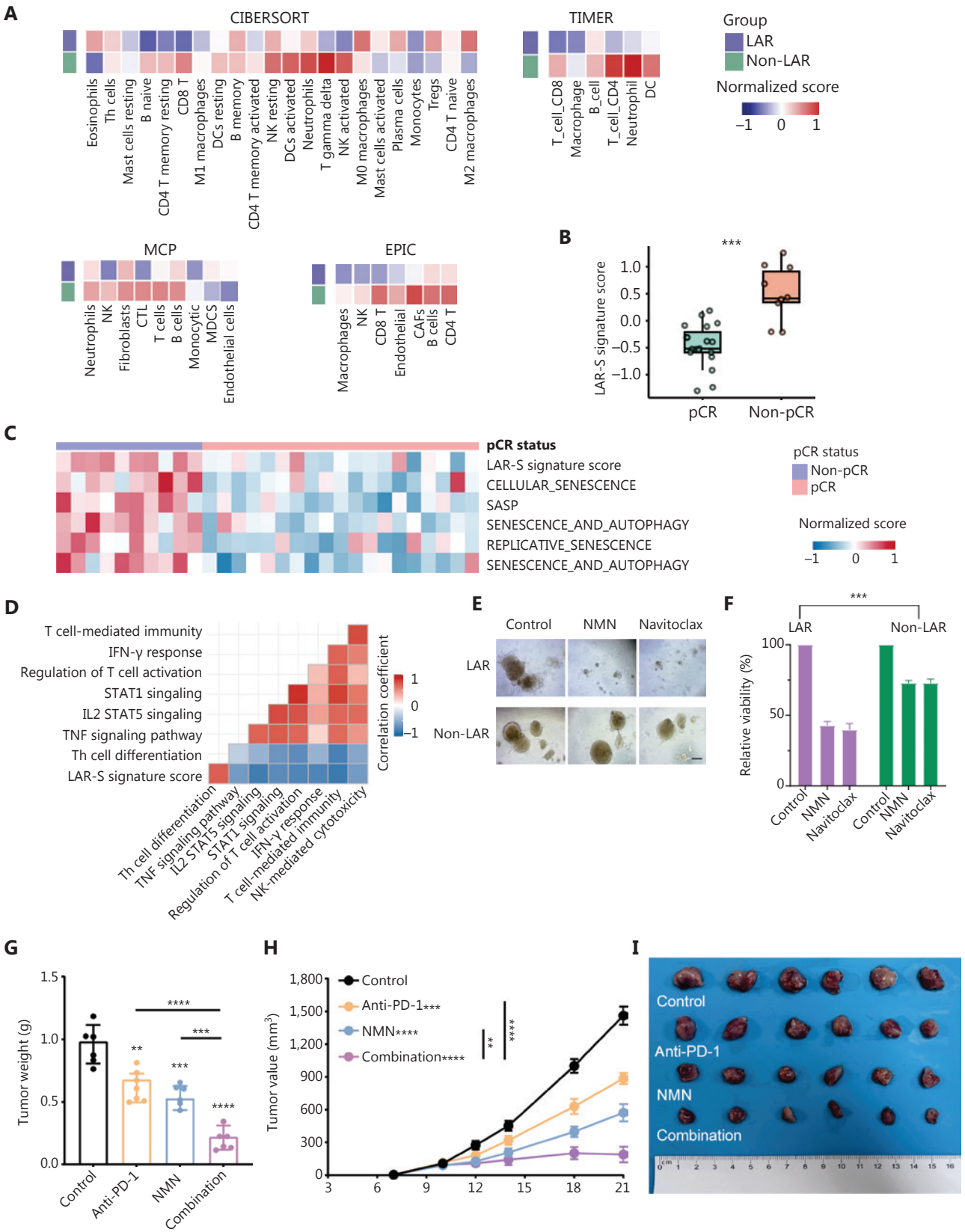

A
CIBERSORT
Eosinophils
Th cells
Mast cells resting
B naive
CD4 T memory resting
CD8 T
M1 macrophages
DCs resting
B memory
CD4 T memory activated
NK resting
DCs activated
Neutrophils
T gamma delta
NK activated
M0 macrophages
Mast cells activated
Plasma cells
Monocytes
Tregs
CD4 T naive
M2 macrophages
TIMER
T_cell_CD8
Macrophage
B_cell
T_cell_CD4
Neutrophil
DC
Group
LAR
Non-LAR
Normalized score
−1 0 1
MCP
Neutrophils
NK
Fibroblasts
CTL
T cells
B cells
Monocytic
MDCS
Endothelial cells
EPIC
Macrophages
NK
CD8 T
Endothelial
CAFs
B cells
CD4 T
B
***
LAR-S signature score
1.0
0.5
0.0
−0.5
−1.0
pCR
Non-pCR
C
pCR status
LAR-S signature score
CELLULAR_SENESCENCE
SASP
SENESCENCE_AND_AUTOPHAGY
REPLICATIVE_SENESCENCE
SENESCENCE_AND_AUTOPHAGY
pCR status
Non-pCR
pCR
Normalized score
−1 0 1
D
T cell-mediated immunity
IFN-γ response
Regulation of T cell activation
STAT1 singaling
IL2 STAT5 singaling
TNF signaling pathway
Th cell differentiation
LAR-S signature score
Correlation coefficient
1
0
−1
Th cell differentiation
TNF signaling pathway
IL2 STAT5 signaling
STAT1 signaling
Regulation of T cell activation
IFN-γ response
T cell-mediated immunity
NK-mediated cytotoxicity
E
Control
NMN
Navitoclax
LAR
Non-LAR
F
***
LAR
Non-LAR
Relative viability (%)
100
50
0
Control
NMN
Navitoclax
Control
NMN
Navitoclax
G
Tumor weight (g)
1.5
1.0
0.5
0.0
****
***
**
***
****
Control
Anti-PD-1
NMN
Combination
H
Tumor value (mm3)
1,800
1,500
1,200
900
600
300
0
3
6
9
12
15
18
21
Control
Anti-PD-1***
NMN****
Combination****
**
****
I
Control
Anti-PD-1
NMN
Combination

Figure 6 The LAR-S correlates with an immunosuppressive phenotype and implicates sensitivity of PD-1 blockade. (A) Heatmap comparing the relative abundance of TME immune cell infiltrates between LAR and non-LAR subtypes in the FUSCC-TNBC cohort, based on CIBERSORT, EPIC, MCP and TIMER. *P* values were calculated using the Wilcoxon rank-sum test and adjusted for multiple testing using the BH method. (B) Boxplot comparing the LAR-S scores between pCR and non-pCR patient groups in the I-SPY 2 cohort. (C) Heatmap displaying the ssGSEA score of the senescence-associated signature in the I-SPY 2 cohort, stratified by pCR *vs.* non-pCR. (D) Heatmap illustrating the correlation coefficients between the LAR-S score and the immune pathway signature in the pCR patient groups. (E) Representative brightfield images of PDOs on day 7 after drug treatment. NMN, 1 mM; navitoclax, 1 μM. (F) Therapeutic response of LAR PDOs following treatment with a senescence inhibitor. Response is shown as relative cell viability. (G) Endpoint tumor weight for LAR xenografts, treated with vehicle control, NMN, anti-PD-1 antibody, or the combination therapy. (H) Tumor growth curves for LAR xenografts in mice. (I) Representative tumor images for LAR xenografts in mice. TME, tumor microenvironment; pCR, pathologic complete response; PDO, patient-derived organoids. Significance levels are denoted as follows: ns, not significant; **P* < 0.05; ***P* < 0.01; ****P* < 0.001; *****P* < 0.0001. Scale bar, 200 μm.

(RRP8), processes that are increasingly implicated in stress responses and senescence programs. The inclusion of RRP8 reflects the metabolic reprogramming required to sustain the highly secretory, senescent phenotype observed in the TNBC LAR subtype. Thus, the LAR-S signature serves not merely as a statistical tool but as a functional surrogate for the metabolic and inflammatory machinery driving this specific subtype. The LAR-S signature accurately identifies the high-risk, senescent phenotype, and as demonstrated in the I-SPY 2 trial data, patients in the non-pCR group had significantly higher LAR-S scores (**Figure 6B**). The signature was negatively correlated with T-cell mediated immunity and IFN-γ response pathways (**Figure 6D**). However, our analysis of the I-SPY 2 cohort was limited by the availability of granular clinical data. Following the validation strategy described in recent studies[25], we focused on the biological association between the molecular signature and therapeutic response. While this approach supports the predictive potential of LAR-S, future prospective trials with strictly matched baselines are warranted to fully rule out confounding effects.

This direct link between senescence, immune suppression, and therapeutic resistance forms the basis of our novel therapeutic proposal. We proposed that pharmacologic modulation of the senescent state could reverse the immune-cold phenotype and resensitize LAR tumors to immunotherapy. LAR patient-derived organoids showed clear dependence on the senescent program *in vitro* because treatment with a senescence-modulating agent markedly suppressed growth (**Figure 6E and 6F**). The *in vivo* experiments demonstrated a strong synergy between the senescence-modulating NAD^+ precursor, NMN, and anti-PD-1 blockade. Although either agent alone afforded only modest tumor control, the combination induced profound and sustained tumor regression (**Figure 6G and 6I**). Mechanistically, the synergy between NMN and anti-PD-1 therapy is driven by the reversal of the senescence-associated immunosuppressive microenvironment. Our validation experiments using flow cytometry demonstrated that NMN treatment dampens the pro-inflammatory SASP, which correlates with a marked reduction in M2-like macrophage polarization and a robust restoration of $CD8^+$ T cell infiltration (**Figure S2**). This reprogramming effectively converts the "cold" immune landscape of LAR tumors into an immunologically "hot" state, thereby overcoming intrinsic resistance to checkpoint blockade. Furthermore, this strategy holds translational potential beyond LAR subtype of TNBC. This concept is consistent with emerging evidence from other malignancies, in which targeting senescent cells or modulating senescence-associated pathways enhances $CD8^+$ T cell infiltration, alleviates immunosuppression, and improves the efficacy of immune checkpoint blockade in senescence-related immune-cold tumors[39-43]. These data provide preclinical proof-of-concept that therapeutically targeting senescence can overcome immune evasion in LAR TNBC, in agreement with emerging evidence that senescence-directed interventions reprogram the SASP-rich, immunosuppressive TME and thereby enhance the efficacy of ICIs.[44,45].

In conclusion, the current study deciphered the complex and paradoxic biology of the TNBC LAR subtype. We have identified two distinct and actionable therapeutic vulnerabilities. For the subset of patients with *ERBB2* mutations, we have provided functional evidence supporting the use of specific TKIs. For the broader, chemo- and immune-resistant LAR population, we identified cellular senescence as a core phenotypic driver. We demonstrated that this senescent state is not only a marker of poor prognosis but also a key mechanism of immune evasion that can be therapeutically exploited. Our machine learning-derived LAR-S signature provides a much-needed clinical tool to identify patients who would be prime candidates for this novel combination strategy, potentially expanding this therapeutic option beyond the LAR subtype to any senescent, immune-cold tumor. This work lays the foundation for future clinical trials aimed at targeting senescence to unlock the potential of immunotherapy for these refractory cancers.

Conclusions

In summary, this study revealed that the TNBC LAR subtype is driven by two distinct yet targetable mechanisms:

ERBB2 kinase domain mutations; and a senescence-mediated, immune-suppressed phenotype. Functional and preclinical evidence demonstrated that *ERBB2* mutations confer sensitivity to specific TKIs, while a senescence-modulating agent synergizes with anti-PD-1 therapy to overcome resistance. The LAR-S signature offers a clinically applicable biomarker to identify patients who may benefit from these precision combination strategies, providing a translational foundation for future therapeutic development in this refractory TNBC subtype.

Grant support

This work received funding from the Ministry of Science and Technology of China (Grant Nos. 2023YFF1205003, 2023YFF0613304, and 2023YFC3402504), the National Key R&D Program of China (Grant No. 2023YFF0613300, 2023YFF1205003), and the National Natural Science Foundation of China (Grant Nos. 82473499, 82272957, and 82303735).

Conflict of interest statement

No potential conflicts of interest are disclosed.

Author contributions

Conceived and designed the analysis: Zhiming Shao, Xin Hu, Yizhou Jiang.
Collected the data: Yaxin Zhao, Ying Wang.
Contributed data or analysis tools: Yaxin Zhao.
Performed the analysis: Yaxin Zhao.
Wrote the paper: Yaxin Zhao, Han Wang.

Data availability statement

The data generated in this study are available upon request from the corresponding author.

References

1. Bianchini G, De Angelis C, Licata L, Gianni L. Treatment landscape of triple-negative breast cancer — expanded options, evolving needs. Nat Rev Clin Oncol. 2022; 19: 91-113.
2. Schmid P, Adams S, Rugo HS, Schneeweiss A, Barrios CH, Iwata H, et al. Atezolizumab and nab-paclitaxel in advanced triple-negative breast cancer. N Engl J Med. 2018; 379: 2108-21.
3. Lehmann BD, Bauer JA, Chen X, Sanders ME, Chakravarthy AB, Shyr Y, et al. Identification of human triple-negative breast cancer subtypes and preclinical models for selection of targeted therapies. J Clin Invest. 2011; 121: 2750-67.
4. Jiang YZ, Ma D, Suo C, Shi J, Xue M, Hu X, et al. Genomic and transcriptomic landscape of triple-negative breast cancers: subtypes and treatment strategies. Cancer Cell. 2019; 35: 428-40.e5.
5. Masuda H, Baggerly KA, Wang Y, Zhang Y, Gonzalez-Angulo AM, Meric-Bernstam F, et al. Differential response to neoadjuvant chemotherapy among 7 triple-negative breast cancer molecular subtypes. Clin Cancer Res. 2013; 19: 5533-40.
6. Lim B, Seth S, Yam C, Huo L, Fujii T, Lee J, et al. Phase 2 study of neoadjuvant enzalutamide and paclitaxel for luminal androgen receptor-enriched TNBC: trial results and insights into "ARness". Cell Rep Med. 2024; 5: 101595.
7. Traina TA, Miller K, Yardley DA, Eakle J, Schwartzberg LS, O'Shaughnessy J, et al. Enzalutamide for the treatment of androgen receptor–expressing triple-negative breast cancer. J Clin Oncol. 2018; 36: 884-90.
8. Bonnefoi H, Lerebours F, Pulido M, Arnedos M, Tredan O, Dalenc F, et al. Darolutamide or capecitabine in triple-negative, androgen receptor-positive, advanced breast cancer (UCBG 3-06 START): a multicentre, non-comparative, randomised, phase 2 trial. Lancet Oncol. 2025; 26: 355-66.
9. Bose R, Kavuri SM, Searleman AC, Shen W, Shen D, Koboldt DC, et al. Activating HER2 mutations in HER2 gene amplification negative breast cancer. Cancer Discov. 2013; 3: 224-37.
10. Zuo WJ, Jiang YZ, Wang YJ, Xu XE, Hu X, Liu GY, et al. Dual characteristics of novel HER2 kinase domain mutations in response to HER2-targeted therapies in human breast cancer. Clin Cancer Res. 2016; 22: 4859-69.
11. Coppé JP, Desprez PY, Krtolica A, Campisi J. The senescence-associated secretory phenotype: the dark side of tumor suppression. Annu Rev Pathol. 2010; 5: 99-118.
12. Dong Z, Luo Y, Yuan Z, Tian Y, Jin T, Xu F. Cellular senescence and SASP in tumor progression and therapeutic opportunities. Mol Cancer. 2024; 23: 181.
13. Zhou L, DeMarco KD, Murphy KC, Wu Z, Li J, Johnson C, et al. P21-positive senescent stromal cells promote prostate cancer immune suppression and progression that can be reversed by senolytic therapy. Cancer Discov. 2026; 16: 571-91.
14. Chen Q, Jiang K, Bronze MS, Li M, Houchen CW, Zhang Y. Tumor microenvironment and macroenvironment: a new perspective on holistic oncology. Cancer Lett. 2025; 634: 218076.
15. Hammond ME, Hayes DF, Dowsett M, Craig Allred D, Hagerty KL, Badve S, et al. American Society of Clinical Oncology/College of American Pathologists guideline recommendations for immunohistochemical testing of estrogen and progesterone receptors in breast cancer. J Clin Oncol. 2010; 28: 2784-95.
16. Cancer Genome Atlas Research Network; Weinstein JN, Collisson EA, Mills GB, Shaw KR, Ozenberger BA, et al. The Cancer Genome Atlas Pan-Cancer analysis project. Nat Genet. 2013; 45: 1113-20.
17. Curtis C, Shah SP, Chin SF, Turashvili G, Rueda OM, Dunning MJ, et al. The genomic and transcriptomic architecture of 2,000 breast tumours reveals novel subgroups. Nature. 2012; 486: 346-52.
18. Wolf DM, Yau C, Wulfkuhle J, Brown-Swigart L, Gallagher RI, Lee PRE, et al. Redefining breast cancer subtypes to guide treatment

prioritization and maximize response: predictive biomarkers across 10 cancer therapies. Cancer Cell. 2022; 40: 609-23.e6.
19. Gao J, Aksoy BA, Dogrusoz U, Dresdner G, Gross B, Sumer SO, et al. Integrative analysis of complex cancer genomics and clinical profiles using the cBioPortal. Sci Signal. 2013; 6: pl1.
20. Gene Ontology Consortium. The Gene Ontology resource: enriching a GOld mine. Nucleic Acids Res. 2021; 49: D325-34.
21. Ogata H, Goto S, Sato K, Fujibuchi W, Bono H, Kanehisa M. KEGG: Kyoto Encyclopedia of Genes and Genomes. Nucleic Acids Res. 1999; 27: 29-34.
22. Yu G, Wang LG, Han Y, He QY. clusterProfiler: an R package for comparing biological themes among gene clusters. OMICS. 2012; 16: 284-7.
23. Liberzon A, Subramanian A, Pinchback R, Thorvaldsdóttir H, Tamayo P, Mesirov JP. Molecular signatures database (MSigDB) 3.0. Bioinformatics. 2011; 27: 1739-40.
24. Zeng D, Ye Z, Shen R, Yu G, Wu J, Xiong Y, et al. IOBR: multi-omics immuno-oncology biological research to decode tumor microenvironment and signatures. Front Immunol. 2021; 12: 687975.
25. Yang F, Xiao Y, Ding JH, Jin X, Ma D, Li DQ, et al. Ferroptosis heterogeneity in triple-negative breast cancer reveals an innovative immunotherapy combination strategy. Cell Metab. 2023; 35: 84-100.e8.
26. Gong Y, Ji P, Yang YS, Xie S, Yu TJ, Xiao Y, et al. Metabolic-pathway-based subtyping of triple-negative breast cancer reveals potential therapeutic targets. Cell Metab. 2021; 33: 51-64.e9.
27. Liu H, Zhang W, Zhang Y, Adegboro AA, Fasoranti DO, Dai L, et al. Mime: a flexible machine-learning framework to construct and visualize models for clinical characteristics prediction and feature selection. Comput Struct Biotechnol J. 2024; 23: 2798-810.
28. Chen D, Xu L, Xing H, Shen W, Song Z, Li H, et al. Sangerbox 2: enhanced functionalities and update for a comprehensive clinical bioinformatics data analysis platform. iMeta. 2024; 3: e238.
29. Jiang S, Li H, Zhang L, Mu W, Zhang Y, Chen T, et al. Generic Diagramming Platform (GDP): a comprehensive database of high-quality biomedical graphics. Nucleic Acids Res. 2025; 53: D1670-6.
30. Jiang YZ, Liu Y, Xiao Y, Hu X, Jiang L, Zuo WJ, et al. Molecular subtyping and genomic profiling expand precision medicine in refractory metastatic triple-negative breast cancer: the FUTURE trial. Cell Res. 2021; 31: 178-86.
31. Liu Y, Fan L, Ye F, Zhao Y, Zhu Y, Yang Y, et al. Androgen receptor interacts with c-Myc to regulate macrophage-osteoclast axis and drive bone metastasis in triple negative breast cancer. Br J Cancer. 2025; 133: 1776-90.
32. Chica-Parrado MR, Kim GM, Uemoto Y, Napolitano F, Lin CC, Ye D, et al. Combined inhibition of CDK4/6 and AKT is highly effective against the luminal androgen receptor (LAR) subtype of triple negative breast cancer. Cancer Lett. 2024; 604: 217219.
33. Peng WT, Jin X, Xu XE, Yang YS, Ma D, Shao ZM, et al. Inhibition of ACAA1 restrains proliferation and potentiates the response to CDK4/6 inhibitors in triple-negative breast cancer. Cancer Res. 2023; 83: 1711-24.
34. Xie X, Manai M, Rampa DR, Fuson JA, Nakasone ES, Pearson T, et al. Targeting CDK7 enhances the antitumor efficacy of enzalutamide in androgen receptor-positive triple-negative breast cancer by inhibiting c-MYC-mediated tumorigenesis. Mol Cancer Ther. 2025; 24: 870-83.
35. Hamilton E, Shastry M, Shiller SM, Ren R. Targeting HER2 heterogeneity in breast cancer. Cancer Treat Rev. 2021; 100: 102286.
36. Marchiò C, Annaratone L, Marques A, Casorzo L, Berrino E, Sapino A. Evolving concepts in HER2 evaluation in breast cancer: heterogeneity, HER2-low carcinomas and beyond. Semin Cancer Biol. 2021; 72: 123-35.
37. Zeng Q, Gong Y, Zhu N, Shi Y, Zhang C, Qin L. Lipids and lipid metabolism in cellular senescence: emerging targets for age-related diseases. Ageing Res Rev. 2024; 97: 102294.
38. Zhang L, Pitcher LE, Yousefzadeh MJ, Niedernhofer LJ, Robbins PD, Zhu Y. Cellular senescence: a key therapeutic target in aging and diseases. J Clin Invest. 2022; 132: e158450.
39. Lv H, Lv G, Chen C, Zong Q, Jiang G, Ye D, et al. NAD^+ metabolism maintains inducible PD-L1 expression to drive tumor immune evasion. Cell Metab. 2021; 33: 110-27.e5.
40. Zhang R, Chen S, Wang Z, Ye L, Jiang Y, Li M, et al. Assessing the effects of nicotinamide mononucleotide supplementation on pulmonary inflammation in male mice subchronically exposed to ambient particulate matter. Environ Health Perspect. 2023; 131: 77006.
41. Li J, Zhang C, Hu Y, Peng J, Feng Q, Hu X. Nicotinamide enhances Treg differentiation by promoting Foxp3 acetylation in immune thrombocytopenia. Br J Haematol. 2024; 205: 2432-41.
42. Liu J, Zong Z, Zhang W, Chen Y, Wang X, Shen J, et al. Nicotinamide mononucleotide alleviates LPS-induced inflammation and oxidative stress *via* decreasing COX-2 expression in macrophages. Front Mol Biosci. 2021; 8: 702107.
43. Wada H, Otsuka R, Germeraad WTV, Murata T, Kondo T, Seino KI. Tumor cell-induced macrophage senescence plays a pivotal role in tumor initiation followed by stable growth in immunocompetent condition. J Immunother Cancer. 2023; 11: e006677.
44. Ruscetti M, Morris JP 4th, Mezzadra R, Russell J, Leibold J, Romesser PB, et al. Senescence-induced vascular remodeling creates therapeutic vulnerabilities in pancreas cancer. Cell. 2020; 181: 424-41.e21.
45. Maggiorani D, Le O, Lisi V, Landais S, Moquin-Beaudry G, Lavallée VP, et al. Senescence drives immunotherapy resistance by inducing an immunosuppressive tumor microenvironment. Nat Commun. 2024; 15: 2435.

Cite this article as: Zhao Y, Wang H, Wang Y, Jiang Y, Hu X, Shao Z. Integrative multi-omic analysis identified *ERBB2* mutations and senescence-driven immune suppression as dual therapeutic targets in LAR triple-negative breast cancer. Cancer Biol Med. 2026; 23: 374-391. doi: 10.20892/j.issn.2095-3941.2025.0691